Humic acids adsorption and decomposition on Mn_2O_3 and α-Al_2O_3 nanoparticles in aqueous suspensions in the presence of ozone

Julia S. Salla[1], Natan Padoin[1], Suélen M. Amorim[1], Gianluca Li Puma[2] and Regina F. P. M. Moreira[*1]

- α- Al_2O_3 nanocatalyst is better than Mn_2O_3 and exhibit a high humic acid removal.
- α- Al_2O_3 nanocatalyst remove humic acid using lower ozone dosage than common catalysts.
- Adsorption of humic acid contributes to its catalytic ozonation.
- Mn_2O_3 decomposes O_3 faster than α- Al_2O_3.

Humic acids adsorption and decomposition on Mn_2O_3 and α-Al_2O_3 nanoparticles in aqueous suspensions in the presence of ozone

Julia S. Salla[1], Natan Padoin[1], Suélen M. Amorim[1], Gianluca Li Puma[2] and Regina F. P. M. Moreira[*1]

[1]Department of Chemical and Food Engineering, Federal University of Santa Catarina, 88040-900, Florianópolis, SC, Brazil.

[2]Environmental Nanocatalysis & Photoreaction Engineering, Department of Chemical Engineering, Loughborough University, Loughborough, United Kingdom

***Corresponding author: Regina de Fatima Peralta Muniz Moreira**

E-mail: regina.moreira@ufsc.br

Tel.: +55-48-3721-2536

Fax: +55-48-3721-9687

Abstract – The removal and decomposition of humic acids (HAs) in the presence of ozone and aqueous suspensions of Mn_2O_3 and α-alumina (Al_2O_3) nanoparticles was investigated. Mn_2O_3 presented lower BET specific surface area (15.6 m^2 g^{-1} vs 45.8 m^2 g^{-1}) but a higher point of zero charge (PZC) (5.9 vs 4.2) than α-Al_2O_3. Solution pH played a key role in the adsorption of HAs and catalytic oxidation on the surface of α-Al_2O_3 and Mn_2O_3 nanoparticles. The adsorption capacity of α-Al_2O_3 at the natural pH of HAs in water (pH 5.5) was up to 2.903 g_{HAs} g^{-1}, but no adsorption occurred onto the Mn_2O_3 nanoparticles, due to the unfavorable surface charge at pH 5.5. In consequence, although Mn_2O_3 was a more efficient catalyst (k_{het} = 0.7 L^{-1} min^{-1} g^{-1}) than α-Al_2O_3 (k_{het} = 0.2 L^{-1} min^{-1} g^{-1}) for the decomposition of O_3, Mn_2O_3 did not exhibited catalytic action during the ozonation of HAs at pH 5.5. Instead, the Mn_2O_3 catalytic action was significant at pH equal to PZC (catalytic rate constant ratio $k_{1\text{-HAcat}}/ k_{1\text{-HA}}$ = 1.562). Overall, α-Al_2O_3 exhibited the highest catalytic removal rate of HAs during ozonation ($k_{1\text{-HAcat}}/ k_{1\text{-HA}}$ = 2.298) due to favorable surface charge and larger specific surface area. The main mechanism for HAs removal in the presence of α-Al_2O_3 involves simultaneous adsorption of both HAs and O_3, the reaction of ozone from the bulk solution and the catalytic decomposition of HAs on the solid surface by ROS, through complex series-parallel reactions. The α-Al_2O_3 dosage up to 0.5 g L^{-1} required to remove HAs by catalytic ozonation was significantly lower than in other studies employing granular activated carbon, iron coated zeolite or γ-alumina catalysts.

Keywords: Ozonation; adsorption, manganese oxide, aluminum oxide, humic acid.

1. Introduction

The removal of natural organic matter (NOM) is one of the main goals in drinking water treatment, since NOM can lead to undesirable color, taste and odor, as well as bacterial regrowth in water distribution systems. In aqueous solution, NOM is a complex mixture of heterogeneous organic compounds with different molecular sizes, structures and functionalities. Approximately 80% of NOM comprises humic acids (HAs) with high molecular weight [1,2]. Since NOM can react with the most common disinfection agents used in water treatment (e.g. chlorine, chlorine dioxide or chloramines) to yield hazardous disinfection byproducts, such as N-nitrosodimethylamine [3] or trihalomethane [4], NOM must be removed prior to water disinfection. In general, the effectiveness of common oxidants on the destruction of the byproducts generated from NOM in drinking water treatment follows the order: ozone (O_3) > chlorine > chlorine dioxide ~ UV [3].

Ozonation is considered an effective technology for the treatment of water for public supply, wastewater and industrial effluents, due to its high capacity for oxidation, removal of color and odor and disinfection from pathogens [5]. The ozonation of HAs causes several structural modifications, which contribute to the removal of color and the reduction of absorption of visible light. Ozonation also decreases the total organic carbon (TOC) of the water, the content of high molecular weight compounds and results in an increase in the oxygenated organic molecules [6].

Although the ozonation of water at circumneutral and alkaline pH generates hydroxyl radicals ($^{\bullet}OH$), which is a highly reactive and nonselective oxidant, other radical oxygen species (ROS) can also be generated through the combinations of ozone with catalysts, with UV radiation or with other oxidants such H_2O_2 [7]. Ozonation at acidic pH, generally, is not an efficient process for the complete removal of the

dissolved organic matter, due to the selective nature of ozonation reactions towards electron rich polar compounds, and as a result of the low solubility of ozone in water [8].

A more efficient water treatment process is catalytic ozonation, which has successfully been applied for the degradation of aqueous organic compounds, such as aromatic hydrocarbons, organic acids, pesticides, pharmaceuticals, and dyes [8,9]. A wide range of materials have been used as catalysts, notably activated carbon [2,10], Al_2O_3 [9,11,12], manganese oxides [13] and other metallic oxides [2,14–18]. However, due to the generally low levels of catalytic activity of these materials, high catalyst doses are often required (up to 10 g L^{-1}) [2,9,14], in order to effectively treat the water. The use of such very high catalyst concentrations in industrial scale water treatment is often uneconomical. Among the catalysts used for the decomposition of ozone, manganese and aluminum oxides are of interest due to their generally low cost, abundance, low toxicity and high catalytic activity when applied in combination with other oxidative processes [19]. However, contradictory results have been reported regarding the mechanism of chemical decomposition of ozone on these catalysts [2,9,11,18,20–23], the rate of production of hydroxyl radicals [24–26], the role of the adsorption of pollutants onto their surface [9], and the effect of alkaline impurities present on the catalyst surface [18]. The false catalytic activity of alumina has been ascribed to the presence of impurities which increase the pH of the water [18]. In addition, the role played by rate of adsorption of the water contaminants in catalytic ozonation is rarely discussed.

In this study, the catalytic role played by Mn_2O_3 and α-Al_2O_3 nanoparticles in aqueous suspensions is investigated for the removal of HAs, in the presence and in the absence of ozone. HAs were selected as representative species of the NOM in drinking water supplies. The roles played by adsorption, ozone decomposition, attack of ozone from the bulk solution and catalytic decomposition on the solid surface, on the kinetics of humic acids removal is examined, and clear evidence of the catalytic effect exerted by the α-Al_2O_3 nanoparticles is demonstrated.

2. Experimental

2.1. Materials

The commercial sample of humic acids (HAs) used in all experiments was purchased from Sigma-Aldrich (CAS 1415-93-6). Homogeneous aqueous stock solutions were prepared by adding 200 mg of HAs to 1.0 L of distilled deionized water, following by ultrasonic sonication (60 min).

The Mn_2O_3 and α-Al_2O_3 nanoparticles with average particle diameter of 40-60 nm were obtained from SkySpring Nanomaterials (USA). All other chemicals were of analytical grade and used without further purification.

2.2. Characterization of catalysts

The specific surface area, pore diameter distribution and pore volume of the catalysts (α-Al_2O_3 and Mn_2O_3) were determined using a Quantachrome Autosorb-3b BET surface area analyzer at -196°C. Prior to the analysis, the samples were degassed for 2 h at 300 °C under vacuum. The point of zero charge (pH_{pzc}) of the Mn_2O_3 and α-Al_2O_3 nanoparticles was obtained by measurements of the zeta potential at different pH values (3.0-11.0) performed on a Stabino-Nanoflex analyzer.

The composition of the solids before and after the kinetic runs was determined through FTIR analysis using an Agilent Technologies spectrophotometer (model Cary 600). The particle size and morphology of the nanoparticles were examined by field emission gun scanning electron microscopy (FEG-SEM) and by transmission electron microscopy (TEM). SEM and TEM analyses were performed using JEOL JSM-6701F and JEOL JEM-1011 microscopes, respectively. The crystallographic composition of the nanoparticles was examined by X-ray diffraction (XRD) analysis, carried out on a Philips X-Pert diffractometer, with a scan of 0.038° s^{-1} and Cu Kα radiation. The oxidation state and surface composition of the nanoparticles were assessed through X-ray photoelectron spectroscopy (XPS) analysis of the samples before and after the kinetic runs. The XPS analysis of the nanoparticles was performed using a hemispheric VSW HA-100 analyzer.

2.3. Experimental setup

2.3.1 Humic acids adsorption onto Mn_2O_3 and α-Al_2O_3 nanoparticles in absence of ozone

The adsorption of humic acids onto the nanoparticles (Mn_2O_3 or α-Al_2O_3) was determined through experiments performed at room temperature (25 ºC). Known amounts of nanoparticles (25 - 250 mg) were added to flasks containing 250 mL of an aqueous solutions of HAs with a fixed initial concentration of 50 mg L^{-1}. The pH of the aqueous suspension, measured with a Quimis Q 400A pH meter, was maintained at 5.5 in all experimental runs.

Aliquots of the liquid phase, withdrawn at various contact times, were filtered and analyzed by spectrophotometry (Shimadzu, UV-Vis 1650PC) at 254 nm to determine the residual concentration of HAs. The concentration of HAs was determined

from a calibration curve made in the spectrophotometer with different HA solutions. The concentration of HAs in the aqueous phase reached an equilibrium after approximately 60 min of contact time and the amount of HAs adsorbed onto the solid phase was calculated from the mass balance (Eq. 1).

$$q_e = \frac{V(C_0 - C_e)}{w} \quad (1)$$

where C_0 and C_e (mg·L^{-1}) are the HAs initial and equilibrium concentrations, respectively, V is the solution volume (L) and w is the amount of catalyst (g) added to the system. Langmuir and Freundlich isotherms (Eqs. 2 and 3, respectively) were fitted to the experimental data to model the adsorption process:

$$q_e = \frac{q_m b C_e}{1 + b C_e} \quad (2)$$

$$q_e = k {C_e}^{1/n} \quad (3)$$

where q_m is the maximum humic acids loading (complete monolayer covering), b is the equilibrium adsorption constant and k and n are constants related to the capacity and intensity of adsorption.

2.3.2 *Ozone dissolution and decomposition in water*

The ozonation experiments were carried out in a 2.0 L glass reactor (68 cm high and 8 cm in diameter) kept at ambient temperature and constant stirring (~500 rpm). Ozone generated from high purity oxygen by a corona discharge ozonator ID-5 (O3R Philozon) fitted with an oxygen concentrator was continuously bubbled in the vessel through two air diffusers at a rate of 0.063 m^3 h^{-1}. All the experiments were carried out in duplicate and the average results were reported.

The rate of ozone mass transfer and steady state ozone concentration in the reactor system, in the absence of Mn_2O_3 and α-Al_2O_3, was investigated at different pH, ranging from 4 to 7. Solutions of 0.1 mol L^{-1} NaOH or H_2SO_4 were used to adjust the pH. The impact of the catalyst (α-Al_2O_3 and Mn_2O_3) at low loadings (0.1 and 0.5 g L^{-1}) on the rate of decomposition of ozone was examined at pH 5.5, since this corresponded with the natural pH of the humic acid aqueous solution. In a typical experiment, ozone was bubbled into distilled water with or without nanoparticles until the medium reached a steady-state ozone concentration. Samples withdrawn at regular time intervals were analyzed spectrophotometrically at 258 nm in a Shimadzu UV-Vis 1650PC spectrophotometer to determine the residual dissolved ozone concentration. The concentration of dissolved ozone in water was determined from the Beer-Lambert law, considering the molar extinction coefficient of ozone (2950 M^{-1} cm^{-1} at 258 nm) [27]. The solid particles, when present, were removed from the samples by filtering through a PVDF membrane (Millipore, 0.22 μm pore size) prior to the spectrophotometric analyses.

The mass transfer and solubility parameters of ozone in the aqueous medium were determined by fitting the solution of the mass balance equation of ozone absorption and decomposition (Eq. 4) to the experimental data.

$$\frac{dC_{O_3}}{dt} = k_L a\left(C_{sat} - C_{O_3}\right) - k_{1-O3} C_{O_3} \quad (4)$$

where C_{sat} (mg L^{-1}) is the saturation concentration of O_3, C_{O_3}(mg L^{-1}) is the concentration of dissolved O_3, $k_L a$ (min^{-1}) is the volumetric mass transfer coefficient of O_3 and k_{1-O3} (min^{-1}) is the decomposition constant of O_3 given by Eq. 5 [28,29]:

$$k_{1-O3} = k_d + w\, k_{het} \quad (5)$$

where w (g L^{-1}) is the catalyst concentration, k_{het} (min^{-1}) is the rate constant for the catalytic decomposition of ozone, k_d (min^{-1}) is the rate constant for the non-catalytic decomposition of ozone.

Different kinetic equations have been proposed to evaluate k_d (min^{-1}) [28,30,31]. Considering the range of applicability of the different equations, the k_d value was estimated according to Sullivan and Roth [28,32] (Eq. 6), that is applicable in the region $2 \leq pH \leq 8$ and $276.7 \leq T \leq 333.2$ K:

$$k_d = 9.811 \cdot 10^7 [OH^-]^{0.123} \exp\left[-\frac{5606}{T}\right] \quad (6)$$

where $[OH^-]$ is the concentration of hydroxyl ions and T is the temperature (K).

The model used in this study (Eq. 4 - 6) considers that ozone is absorbed in water and simultaneously decomposes through reaction with the hydroxyl ions (non-catalytic decomposition) and through reaction on the surface of the nanoparticles (catalytic decomposition). Eq. (4) was discretized through the Euler's method and implemented in Matlab® (MathWorks, The MathWorks Inc., MA) to determine the model parameters. The value of each parameter was obtained by minimizing the error between the model predictions and the experimental data.

2.3.3 Humic acid removal in the presence or absence of ozone and/or catalyst

The kinetics of HAs removal, in the presence or absence of ozone and/or catalyst, was investigated in the experimental setup described above using 1.0 L of an aqueous solution of HAs (50 mg L^{-1}). The ozonation of HAs, in the absence of solid nanoparticles, was investigated in the range $4.0 < pH < 10.0$, while in the presence of Mn_2O_3 or α-Al_2O_3 nanoparticles (0, 0.1 or 0.5 g L^{-1}) it was performed at pH 5.5, the natural pH of HAs in water. The experiments were performed under vigorous stirring

and continuous ozone bubbling. Aliquots of the liquid phase (3 mL) withdrawn at regular time intervals were filtered and analyzed by UV/vis spectrophotometry.

A small amount (0.1 mL) of a solution of sodium sulfite (3 g L^{-1}) was added to all aliquots immediately after sampling to suppress the residual dissolved ozone and further chemical reactions. The decay of HAs over the time (*t*) was described according to a pseudo-first order kinetic model (Eq. 7).

$$-\ln\frac{[HA]}{[HA]_0} = k_1\, t \qquad (7)$$

The stability of the nanoparticles (α-Al_2O_3) was investigated by reusing the solid in consecutive experiments performed under the same conditions. After every cycle, the nanoparticles were removed by filtration through a PVDF membrane (Millipore, 0.22 μm pore size) and dried at 60 °C for 24 h before reuse in the next experiment. A fresh HAs solution was used in each cycle.

3. Results and Discussion

3.1. Characterization of α-Al_2O_3 and Mn_2O_3 nanoparticles

The results of the textural characterization of the solids are presented in Table 1. The specific surface areas, determined by the BET method, were typical of nanomaterials [26,33]. Mn_2O_3 surface area and pore volume were significantly lower that the values for α-Al_2O_3. The pore diameter distribution shown in Table 1 was determined by the Barret, Joyner and Halenda (BJH) method [34]. According to IUPAC classification, the average pore diameters of the nanoparticles were characteristic of mesoporous materials [35].

Figure 1 shows the N_2 adsorption/desorption isotherms of Mn_2O_3 and α-Al_2O_3 at 77 K. Clearly, the two curves were similar and no hysteresis was observed. Both isotherms were type III according to the IUPAC classification, indicating multilayer adsorption onto non-porous, macroporous or mesoporous materials [36].

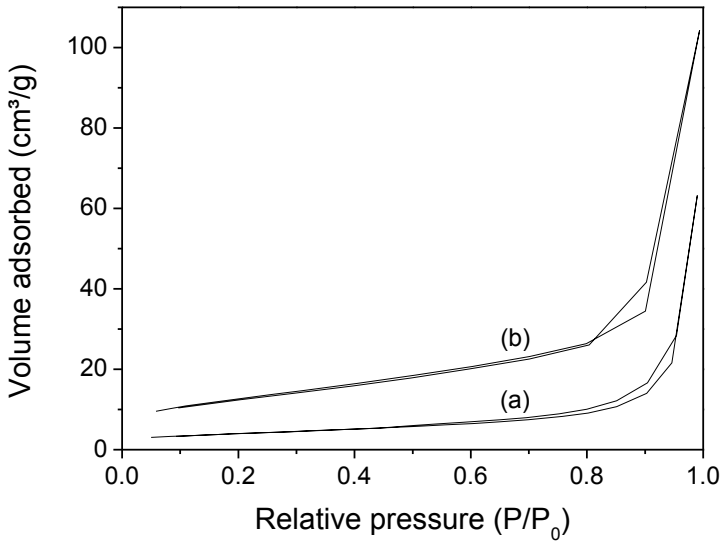

Figure 1 – N_2 adsorption/desorption isotherms at 77K using (a) Mn_2O_3 and (b) Al_2O_3.

The values for the point of zero charge (PZC) of the Mn_2O_3 and Al_2O_3 nanoparticles are shown in Table 1 and Figure S-1. These represent the pH value where negative ($[MO^-]$) and positive ($[MOH_2^+]$) surface concentrations are equal, i.e., the surface charge is zero. The catalyst surface charge is negative at pH > PZC and positive at pH < PZC. The PZC of Al_2O_3 was well below the natural pH 5.5 of HAs in solution (the pH applied in the catalytic ozonation experiments), therefore the surface of Al_2O_3 was negatively charged during the ozonation experiments, while the net surface charge of Mn_2O_3 was slightly positive at the pH 5.5.

Table 1 – Textural characterization and the point of zero charge of Mn_2O_3 and α-Al_2O_3.

	Mn_2O_3	α-Al_2O_3
BET area ($m^2\ g^{-1}$)	15.6	45.8
Pore volume ($cm^3\ g^{-1}$)	0.008	0.162
Pore diameter distribution (nm)	3.78	23.20
Point of zero charge - pH_{pzc}	5.9	4.2
Cristallyte size (nm)*	15.9	41.7

* Calculated by Scherrer Equation [37].

Figure S-2 (Supplementary Material) shows the FTIR spectra of the α-Al_2O_3 and Mn_2O_3 nanoparticles before and after the ozonation of HAs. Clearly, the vibrational absorption spectra of the aluminum and manganese oxide do not show a significant change caused by the ozonation of the HAs, indicating that the nanoparticles remained stable and that their chemical composition was maintained during the reactive catalytic process.

The large absorption bands at 3450 cm^{-1} observed in Figure S-1, were due to the symmetric/asymmetric stretching of the OH group, indicating the presence of water in the structure of the compounds. In Figure S-2 (a), the peak observed in the region around 1100 cm^{-1} can be attributed to the Al^{3+} and O^{2-} groups at the vibrational surface of Al-O. Furthermore, the bands encountered at 495 cm^{-1} can be assigned to the angular deformation of the A-O bonds, while the bands at 550 cm^{-1} and 950 cm^{-1} relate to the symmetrical flexion of O-Al-O [38].

Figure S-1 (b) shows absorption bands between 700 cm^{-1} and 500 cm^{-1}, which can be attributed to Mn-O and Mn-O-Mn vibrations, respectively [39]. Moreover, the peaks observed at 1550 cm^{-1} and 3500 cm^{-1} can be related to the symmetric/asymmetric stretching of the OH group associated with the water content in the compound [40].

The FEG-SEM and TEM results for the morphological analysis of the Al_2O_3 and Mn_2O_3 nanoparticles are shown in Figure 1 and 2. Overall, both materials presented a heterogeneous morphology and regions with irregular particle size. In particular, the α-

Al_2O_3 appeared as coalescent particles with a platelet format, typically encountered in the structure of α-Al_2O_3 [41,42]. In contrast, the Mn_2O_3 particles were circular well-organized grains. The particles of Mn_2O_3 and α-Al_2O_3 formed aggregates (Figure 2) with diameters of 20-60 nm and less than 20 nm (Figure 3), respectively.

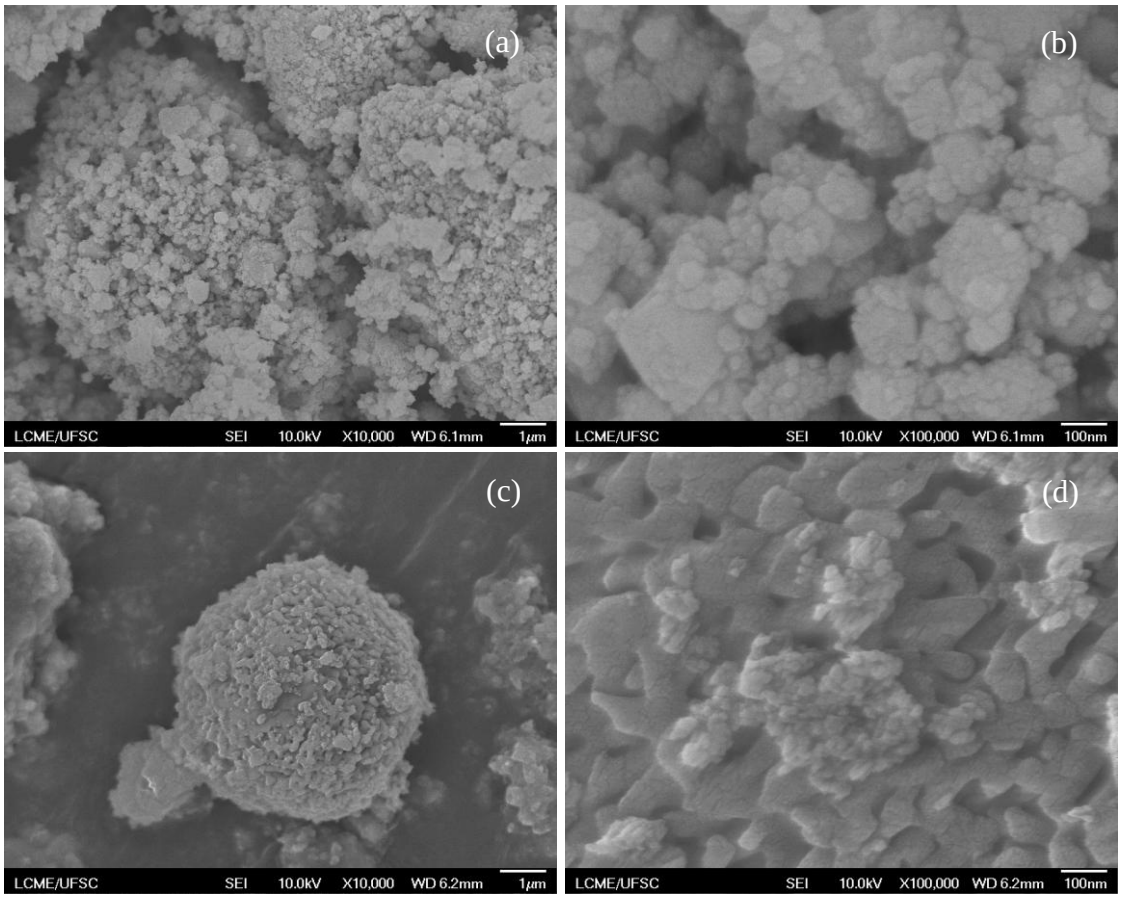

Figure 2 – FEG-SEM images for Mn_2O_3 (a, b) and α-Al_2O_3 (c, d) nanoparticles.

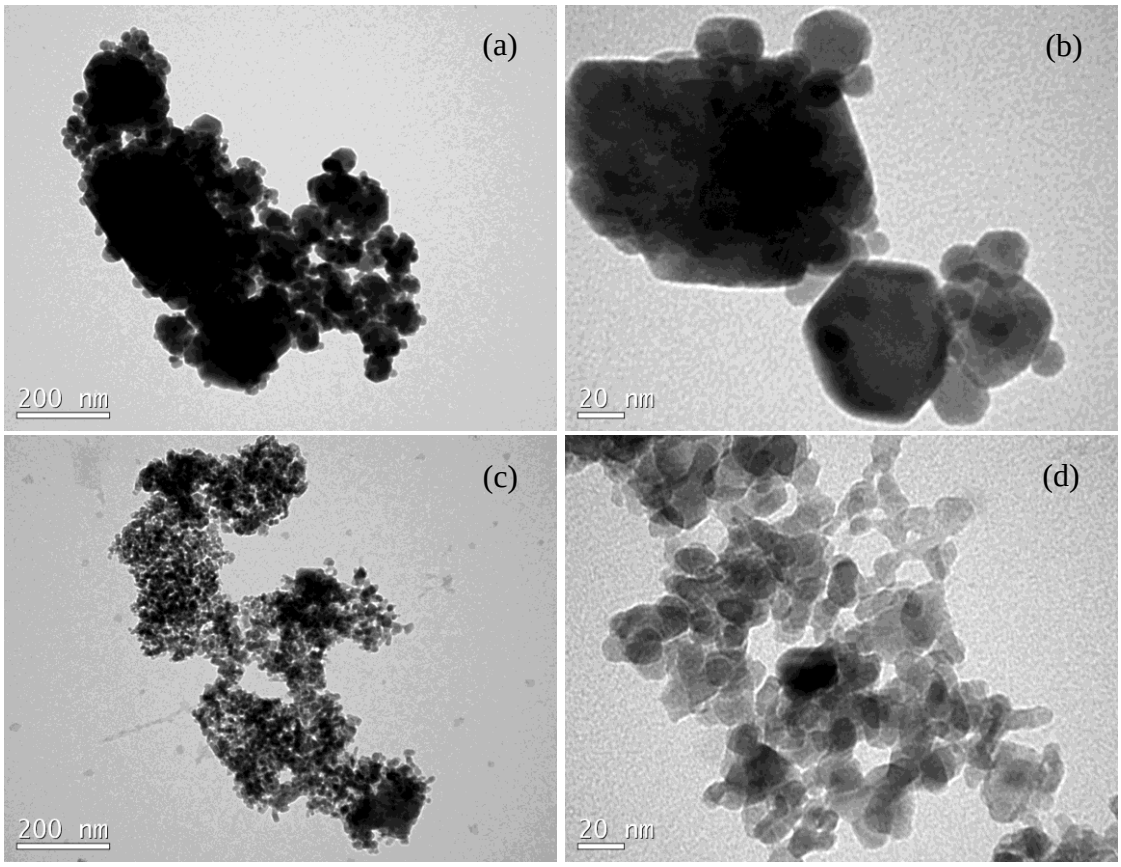

Figure 3 – TEM images for Mn_2O_3 (a, b) and α-Al_2O_3 (b, c) nanoparticles.

The X-ray diffraction patterns of the Mn_2O_3 or α-Al_2O_3 nanoparticles (Figure S-3, Supplementary Material) showed the formation of crystalline phases in both solids. The characteristic diffraction peaks of Mn_2O_3 nanoparticles were identified at 2θ = 23.13º, 32.95º, 38.23º, 45.16º, 49.34º, 55.17º and 65.77º (JCPDS-89-4836) [43,44]. The diffraction peaks of α-Al_2O_3 nanoparticles appeared at 2θ = 25.57º, 35.14º, 37.76º, 43.33º, 52.53º, 57.47º, 61.27º, 66.49º, 68.18º and 76.84º (JCPDS-88-0826), as also reported by Kim et al. [42]. However, diffraction peaks associated with $Al(OH)_3$ (2θ = 18.68º, 20.25º and 45.57º, JCPDS-15-0138) were also observed, which indicated the presence of residual traces of this compound during the synthesis process of α-Al_2O_3.

The crystallite sizes (Table 1) calculated according to Scherrer equation [37] were near to the particle size informed in the supplier data sheet.

The oxidation state of the α-Al_2O_3 and Mn_2O_3 nanoparticles before and after ozonation process was investigated by XPS and the results are shown in Figure 4 and 5, respectively.

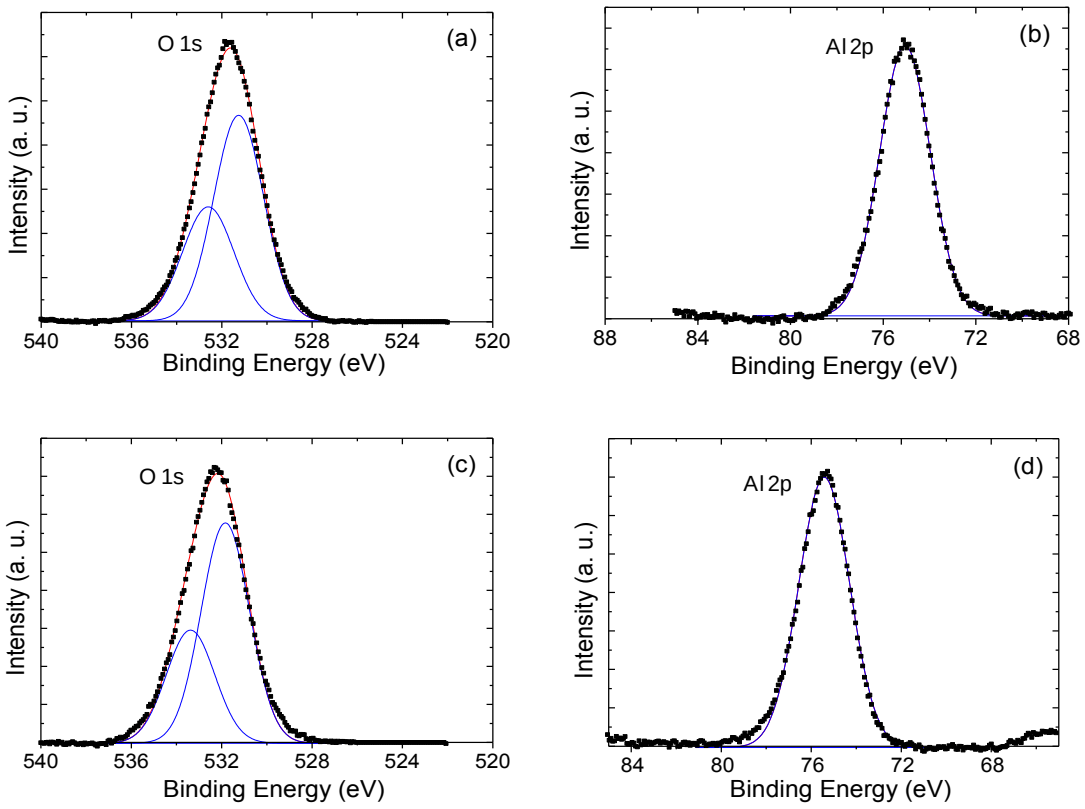

Figure 4 – XPS spectra of O 1s and Al 2p for α-Al_2O_3 nanoparticles before (a, b) and after (c, d) ozonation.

The fresh α-Al_2O_3 sample (Figure 4(a)), showed two contributions to the O 1s signal at 531.2 eV and at 532.6 eV, corresponding to the Al-O bond and to the oxygen of the OH group, respectively [45]. Moreover, the peak at 75 eV observed in Figure 4(b) related to Al 2p and was attributed to Al in the 3+ oxidation state [45].

The peaks at binding energies of 531.8 eV and 533.4 eV observed after ozonation (Figure 4(c)) corresponded to the O_2^- and OH ions, respectively, while the level Al 2p shifted to higher binding energies (75.4 eV) after ozonation (Figure 4(d)) indicating a possible increase in the oxidation state [46].

Figure 5 shows the XPS spectra for the Mn_2O_3 nanoparticles after ozonation. The XPS spectra of the fresh Mn_2O_3 sample can be found in a previously published work of the same research group [47].

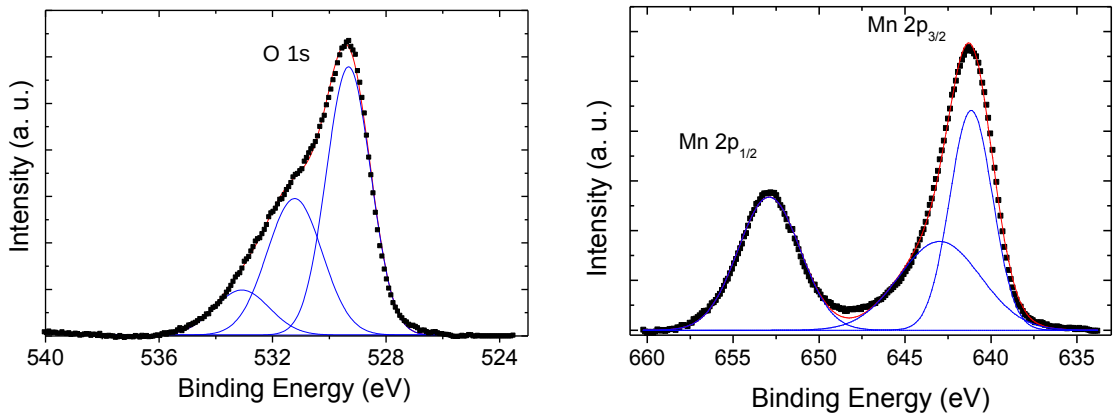

Figure 5 – XPS spectra of O 1s and Mn 2p for Mn_2O_3 nanoparticles after ozonation.

In the O1s region, Figure 5 (a), the XPS spectra of the manganese oxide sample taken after ozonation showed peaks with binding energies of 529.3 and 531.2 eV, due to the Mn-O bond which was also present in the fresh Mn_2O_3 [47], while the peak at 533.1 eV related to the oxygen of the OH group. Moreover, peaks related to the binding energies of 653 eV and 642 eV shown in Figure 5 (b), corresponded to Mn $2p_{1/2}$ and Mn $2p_{3/2}$, respectively [48]. The fresh Mn_2O_3 nanoparticles showed the same peak at 653 eV, but the second peak, related to Mn $2p_{3/2}$, had binding energy of 641 eV [47]. According to Li et al. [33], the peak due to Mn $2p_{3/2}$ can be used to determine the oxidation state of manganese in its oxides. Peaks close to 640, 641 and 642 eV can be

attributed to Mn^{2+}, Mn^{3+} and Mn^{4+}, respectively. Therefore, before ozonation, the Mn_2O_3 nanoparticles were in the 3+ oxidation state and, while after ozonation, the manganese main oxidation states were Mn^{3+} (62.9 at %) and Mn^{4+} (37.1 at %).

The co-existence of two oxidation states Mn^{3+}/ Mn^{4+} on the Mn_2O_3 surface is indicative of electron transfer from the metal oxide to the ozone molecules, which could result in the formation of free radicals ($^{\bullet}OH$, $^{\bullet}O_2H$ and $^{\bullet}O_2^-$) [12,49,50]. This observation might imply faster rate of degradation of HAs, if these were adsorbed onto the solid surface where ozone would be continuously adsorbed and decomposed.

3.2. Absorption and decomposition of ozone in water

The study of ozone decomposition in non-catalytic and catalytic reactions and the aspects of mass transfer are of fundamental importance in the study of ozonation systems applied to water treatment. Mainly because the decomposition of ozone in water and the formation of hydroxyl radicals is directly related to the rate of mass transfer of ozone from the gas to the liquid phase.

Figure 6 shows the kinetics of dissolution of ozone in water at different pH in the absence of catalyst and the impact of catalyst dosage at pH 5.5. The model parameters fitted to the experimental data are shown in Table 2. Clearly, the concentration of ozone in the aqueous medium increased until a steady state was reached, when the ozone absorption rate equaled the sum of the ozone decomposition rate due to reaction with hydroxyl ions (Eq. 9) and the heterogeneous reactions occurring on the solid surface (Eq. 10 – 13) [29].

$$O_3 + OH^- \leftrightharpoons HO_2^- + O_2 \quad (9)$$

$$O_3 + S \leftrightharpoons O_3 \cdot S \quad (10)$$

$$O_3 \cdot S \leftrightharpoons O \cdot S + O_2 \quad (11)$$

$$O_3 + O \cdot S \leftrightharpoons 2O_2.S + O_2 \quad (12)$$

$$O_2 \cdot S \leftrightharpoons 2O_2 + S \quad (13)$$

The reaction sequence of ozone decomposition on oxide surfaces (Eq 10-13) involves the dissociative adsorption of ozone to form an oxygen molecule and atomic oxygen. The reaction of atomic species with gaseous ozone forms an adsorbed peroxide species and gas phase oxygen, and finally the decomposition of the peroxide intermediate produces molecular oxygen [51].

Moreover, the results showed that the ozone equilibrium concentration slightly decreased at more alkaline pH (~15%), Figure 6 (a), due to the higher concentration of OH^- ions in solution, which initiated the decomposition of ozone leading to a chain reaction with the participation of free radicals [52]. Thus, the constant for the non-catalytic decomposition of ozone (k_d), Table 2, increased at higher pH and this translated with an increase in the overall rate of ozone decomposition. In the more acidic medium the decomposition is smaller, since lower concentrations of OH^- ions are available to decompose the O_3 molecule.

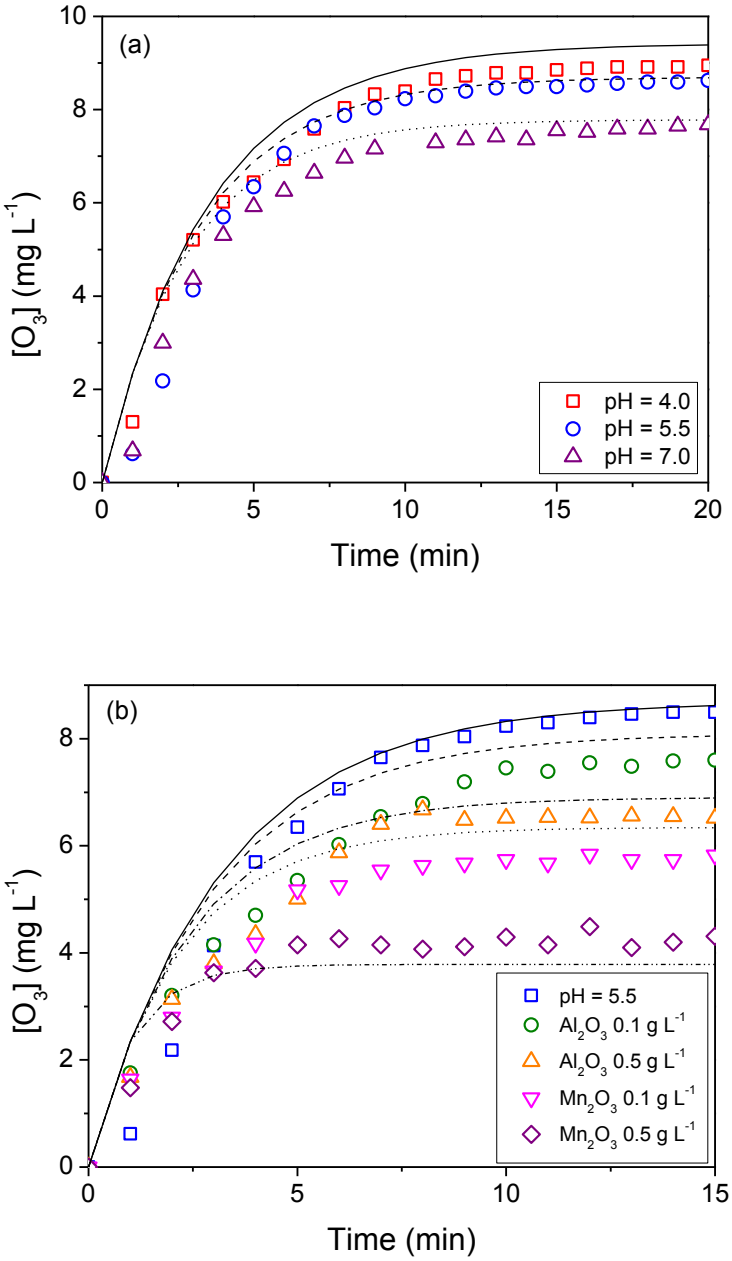

Figure 6 –Dissolved ozone concentration in aqueous phase as a function of reaction time: (a) at different initial values of pH (4.0, 5.5 and 7.0) without catalyst; and (b) with different dosages (0.1 and 0.5 g L^{-1}) of Al_2O_3 or Mn_2O_3 nanocatalysts at pH 5.5 (T = 25 ºC, flow rate of O_3 = 0.063 m^3 h^{-1}). Model predictions (lines) and experimental data (points).

Table 2 –Parameters (k_d, k_La, C_{sat} and C_e) fitted to the experimental data of ozone absorption and decomposition in aqueous medium (T = 25 ºC, flow rate of O_3 = 0.063 $m^3\ h^{-1}$).

pH	Catalyst	Catalyst dosage ($g\ L^{-1}$)	k_d (min^{-1})	k_{het} ($L^{-1}\ min^{-1}\ g^{-1}$)	k_La (min^{-1})	C_{sat} ($mg\ L^{-1}$)	C_e ($mg\ L^{-1}$)
4.0	-	-	0.0391	-	0.21	11.17	9.04 ± 0.09
5.5	-	-	0.0597	-			8.90 ± 0.19
	Mn_2O_3	0.1		0.7			5.92 ± 0.06
		0.5					4.27 ± 0.05
	α-Al_2O_3	0.1		0.2			7.92 ± 0.08
		0.5					6.83 ± 0.13
7.0	-	-	0.0914	-			7.68 ± 0.11

In this study, C_{sat} was considered as an adjustable parameter. However, the value determined from the fitting of the model to the experimental results (11.17 mg L^{-1}) considerably agrees with the literature (11.4 mg L^{-1}) [53].

The rate of decomposition of dissolved O_3 in the water significantly increased (up to 15%) in the presence of catalyst (Figure 6b). At pH 5.5, the neutral or weakly positively charged Mn_2O_3 produced a higher rate of ozone decomposition in comparison to α-Al_2O_3, which is negatively charged at pH 5.5. The net surface charge affects the desorption of the peroxide species $O_2{\cdot}S$ since these have a partial ionic character (O^{2-}, O_2^{2-}) [54], and consequently this facilitates the regeneration of the active sites on the surface of the catalyst. Since the desorption energy of peroxide species ($O_2{\cdot}S$) increases with decreasing surface coverage [54], the desorption of ($O_2{\cdot}S$) from the negatively charge α-Al_2O_3 surface will decrease the desorption rate of O_2 molecules (Eq. 13) and therefore the regeneration rate of the α-Al_2O_3 surface, resulting in slower O_3 decomposition in α-Al_2O_3 than in Mn_2O_3.

The rate constant of catalytic decomposition of ozone (k_{het}) is a function of the hydroxyl ion concentration [29], which is a typical equation commonly found from Langmuir Hinshelwood mechanism. At a constant pH (pH 5.5) the values of k_{het} for

Mn_2O_3 and α-Al_2O_3 are 0.7 and 0.2 L^{-1} min^{-1} g^{-1}, respectively (Table 2). The present study shows clear evidence that α-Al_2O_3 is an effective catalyst to decompose ozone in aqueous phase, although this effect has been associated by some authors [17,18] to the impurities contained in the α-Al_2O_3 that raises the pH of the water. This effect was not evidenced in this study. The only $Al(OH)_3$ impurity in the α-Al_2O_3 (Figure S-3) could contribute to the catalytic effect, but no significant change of the pH was measured after the introduction of the oxide to water due to the acidic character of the solid surface (pH_{pzc} = 4.2) (Table 1).

Moreover, the concentration of ozone at the steady-state decreased as the concentration of the nanocatalysts in the water increased (Figure 6b) giving strong evidence of the catalytic effect of these oxides. Good agreement was found between the kinetic model (Eq. 2 – 4) and the experimental data. The selection of the experimental conditions for the effective removal of HAs with ozone and Mn_2O_3 and α-Al_2O_3 nanoparticles were therefore based on the results of ozone decomposition on the two oxides.

3.5. Ozonation of HAs in water

The kinetics of HAs removal as a function of pH was investigated in the range from 4 to 10 (Figure 7), to determine the impact of ozone decomposition in the absence of nanoparticles. As expected, a higher degradation rate of HAs was observed under alkaline conditions, since the ozonation mechanism follows an indirect route in which the strong $^{\bullet}OH$ radical is produced. However, a relatively high rate of HAs degradation was also observed at acidic pH, as a result of the direct attack of ozone on the electron rich sites in the HAs molecules, such as amines aromatics, olefins, and other polar groups [55]. The reactions of HA with $^{\bullet}OH$ radicals are non-selective, while the

mechanism of reactions of HAs with molecular ozone are selective [29]. The decomposition of HAs with ozone was accompanied by a progressive decrease of pH, due to the formation of acidic fragments [55]. Therefore, the uncompleted removal of HAs observed in Figure 7 could be ascribed to the formation of intermediate acidic compounds recalcitrant to attack by molecular ozone, since at this pH values the concentration of $^{\bullet}OH$ radical would be insignificant.

Overall the results show negligible impact of pH in the interval from 5.5 to 10.0, and a negative impact at pH 4.0, which decreased the HAs removal by approximately 10%. In all cases the removal of HAs was higher than 70%, it approaches 80% at circumneutral pH and reached 87% at highly alkaline pH.

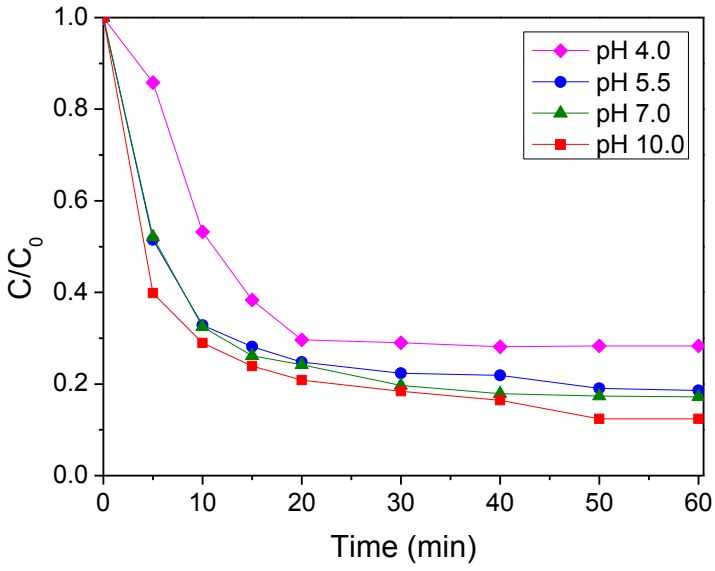

Figure 7 – Kinetics of humic acid ozonation at different initial pHs (T = 25 ºC; flow rate of ozone = 0.063 $m^3\ h^{-1}$; $[HA]_0$ = 50 mg L^{-1}).

3.4. Adsorption of HAs onto α-Al_2O_3 and Mn_2O_3 nanoparticles

The adsorption of HA on α-Al_2O_3 nanoparticles at equilibrium and at pH 5.5 is shown Figure 8, whilst the adsorption on Mn_2O_3 was insignificant (Figure S-4,

Supplementary Material). The equilibrium isotherm of α-Al_2O_3 could be described by the Langmuir or Freundlich models, for which the parameters are shown in the inset of Figure 7.

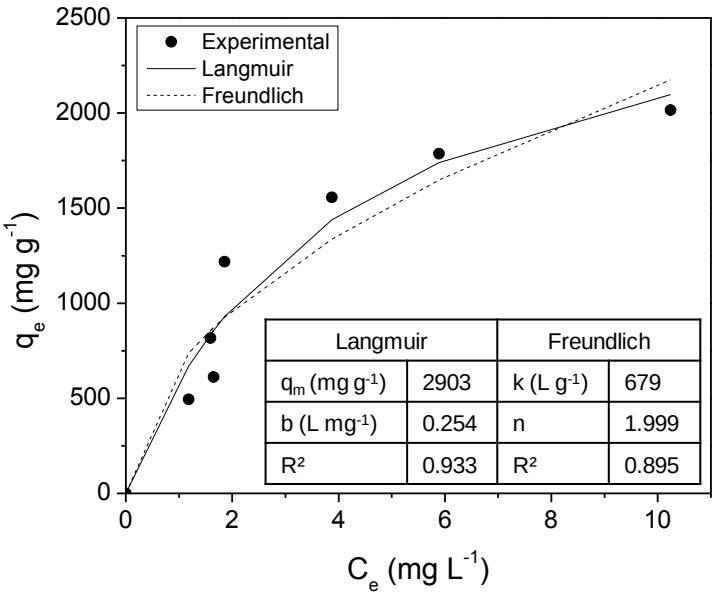

Figure 8 – Adsorption of humic acid onto α-Al_2O_3 nanoparticles (pH = 5.5; T = 25 ºC; $[HA]_0$ = 50 mg L^{-1}) and fitting of Langmuir and Freundlich isotherms. Model predictions (lines) and experimental data (points).

The adsorption of HAs onto α-Al_2O_3 is pH dependent [56]. Although a fractionation of the HAs organic matter remaining in solution could occur as a result of adsorption onto α-Al_2O_3 [56], this effect can be considered negligible in the present study since the HAs concentration adsorbed vastly exceed the limit of 20 mg $g_{\alpha\text{-}Al2O3}^{-1}$ reported in literature at which this phenomenon is considered important [56].

The HAs used in this study presented two pK_a values: one attributed to the OH group (pK_a = 10.2) and the other the related to the COOH group (pK_a = 6.7) [57]. Therefore, the dissolved HAs were mainly in the protonated form under the conditions

adopted in this study (pH 5.5) and could thus be attracted to and adsorbed onto the negatively charged surface of the α-Al_2O_3 nanoparticles. On the other hand, the pH_{zpc} of the Mn_2O_3 nanoparticles was close to that of the aqueous solution (Table 1), thus, only weak interactions could be established between the surface of Mn_2O_3 and the HAs. In addition, both the surface of Mn_2O_3 and the HAs were positively charged at pH 5.5. Therefore, the low surface area of Mn_2O_3 (Table 1) coupled with the weak repulsion forces at the surface of the Mn_2O_3 nanoparticles explains the insignificant extent of HAs adsorption observed. These observations suggest that the reaction mechanism of removal of HAs on α-Al_2O_3 and Mn_2O_3 in the presence of ozone can also be significantly different. α-Al_2O_3 adsorbs a significant fraction of HAs but has lower rate of ozone decomposition, while Mn_2O_3 has very weak interactions with HAs but has a higher rate of ozone decomposition.

3.6 Ozonation of HAs with suspensions of α-Al_2O_3 and Mn_2O_3 nanoparticles

The rate of HAs removal with ozone, at pH 5.5, was nearly the same with or without Mn_2O_3 (Figure 9). Although, Mn_2O_3 did not remove HAs by adsorption, it presented higher catalytic activity than α-Al_2O_3, to decompose ozone in the aqueous phase. In contrast, the removal of HAs with ozone was significantly enhanced by the presence α-Al_2O_3, as a result of the higher rate of HAs adsorption and catalytic decomposition of O_3 on the solid surface. The heterogeneous reaction of HAs with ROS generated at the surface of α-Al_2O_3 plays a key role in the removal process. The kinetics data where fitted by pseudo-first-order model, and the reaction rate constants are shown in Table 3 as function of pH, together with the catalytic rate constant ratio ($k_{1\text{-}HAcat}/k_{1\text{-}HA}$), which is defined as a ratio of the pseudo-first-order rate constant for HA

degradation by catalytic ozonation ($k_{1\text{-HAcat}}$) and the pseudo-first-order rate constant for HA degradation by non-catalytic ozonation ($k_{1\text{-HA}}$).

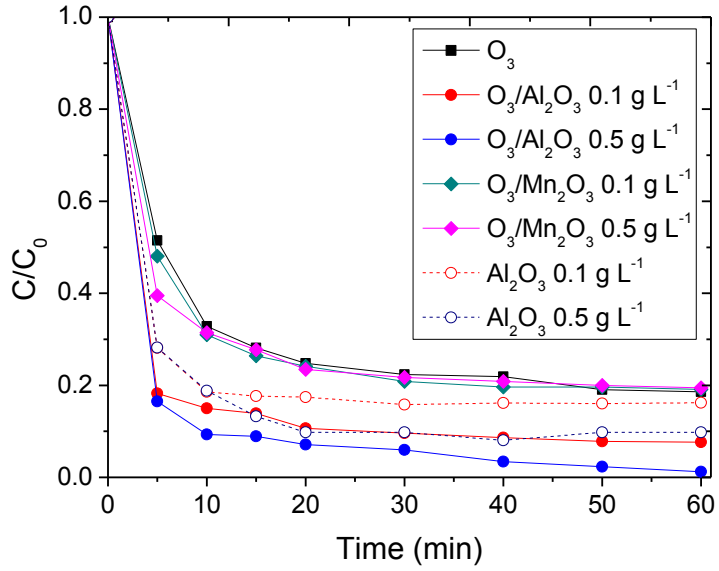

Figure 9 – Kinetics of humic acids ozonation and humic acid adsorption on Mn_2O_3 or α-Al_2O_3 nanoparticles in the presence or absence of ozone (pH = 5.5; T = 25 ºC; $[HA]_0$ = 50 mg L^{-1}; flow rate of ozone = 0.063 m^3 h^{-1}).

Table 3 – Pseudo-first-order specific rate constant for humic acid degradation by non-catalytic ($k_{1\text{-HA}}$) and catalytic ozonation ($k_{1\text{-HAcat}}$) at different pHs and catalyst dosages (T = 25 ºC; flow rate of ozone = 0.063 m^3 h^{-1}; $[HA]_0$ = 50 mg L^{-1}).

pH	Catalyst	Catalyst dosage (g L^{-1})	Pseudo-first-order specific rate constant, min^{-1}	R^2	$k_{1\text{-HAcat}}$/ $k_{1\text{-HA}}$
4.0	-	-	0.056 ± 0.009*	0.925	-
4.2	-	-	0.092 ± 0.012*	0.951	-
	α-Al_2O_3	0.1	0.122 ± 0.023**	0.901	1.326
5.5	-	-	0.114 ± 0.006*	0.991	-
	Mn_2O_3	0.1	0.123 ± 0.008**	0.986	1.079
		0.5	0.129 ± 0.020**	0.933	1.132
	α-Al_2O_3	0.1	0.220 ± 0.042**	0.895	1.930
		0.5	0.262 ± 0.035**	0.949	2.298
5.9	-	-	0.080 ± 0.009*	0.963	-

	Mn_2O_3	0.1	$0.125 \pm 0.017^{**}$	0.949	1.562
7.0	-	-	$0.115 \pm 0.005^{*}$	0.994	-
10.0	-	-	$0.134 \pm 0.016^{*}$	0.954	-

* non-catalytic ozonation, $k_{1\text{-}HA}$; ** catalytic ozonation, $k_{1\text{-}HA}$)

At pH > pH_{pzc} (5.5 > 4.2), the negatively charged surface of the α-Al_2O_3 nanoparticles enabled the adsorption of larger fraction of HAs, therefore, the catalytic rate constant ratio ($k_{1\text{-}HAcat}$/ $k_{1\text{-}HA}$) decreased from 1.930 to 1.326. Moreover, the catalytic effect of Mn_2O_3 on the HAs removal at pH 5.5 was not observed, and no significant difference between the HAs removal with or without Mn_2O_3 nanoparticles was found ($k_{1\text{-}HAcat}$/ $k_{1\text{-}HA}$ ~ 1). As discussed earlier, the repulsive forces between the positively charged Mn_2O_3 surface and the protonated HAs molecules at pH 5.5 argue against a catalytic effect. So, similar mechanisms are involved on the HAs removal by ozone in the presence or in the absence of Mn_2O_3 nanoparticles. However, at the pH_{pzc} of Mn_2O_3 particles (5.9), the catalytic effect becomes significant ($k_{1\text{-}HAcat}$/ $k_{1\text{-}HA}$ =1.562) due to the more favorable conditions for HAs adsorption and the high rate of ozone decomposition on the catalyst surface. As shown in Figure 6b, the α-Al_2O_3 and Mn_2O_3 nanoparticles are effective catalysts for the decomposition of ozone (Reactions 9-13). The lower catalytic activity of α-Al_2O_3 in comparison to Mn_2O_3 does not limit the ability of α-Al_2O_3 to catalytically decompose HAs. The apparent higher HAs decomposition rate observed with α-Al_2O_3 should also be ascribed to the much larger surface area (Table 1) and favorable rate of HAs adsorption, although this last factor can be manipulated by an appropriate selection of pH.

The main mechanism for HAs removal in the presence α-Al_2O_3 nanoparticles can be proposed as the simultaneous adsorption of both HAs and O_3, the reaction of

ozone from the bulk solution and the catalytic decomposition of HAs on the solid surface by ROS, through complex series-parallel reactions.

To support this hypothesis, consecutive reusing cycles of the α-Al_2O_3 catalyst were performed. Each run lasted 60 minutes and the catalyst was reused without any regeneration or specific treatment. A progressive decrease of the pseudo-first-order rate constants (Figure 10) was observed over 4 cycles, indicating a partial saturation of the surface solid by HAs adsorption. This effect maybe associated with a progressive decrease of the amount of free adsorption sites by irreversible chemisorption of HAs and/or its degradation byproducts, which decreases the adsorption capacity for ozone.

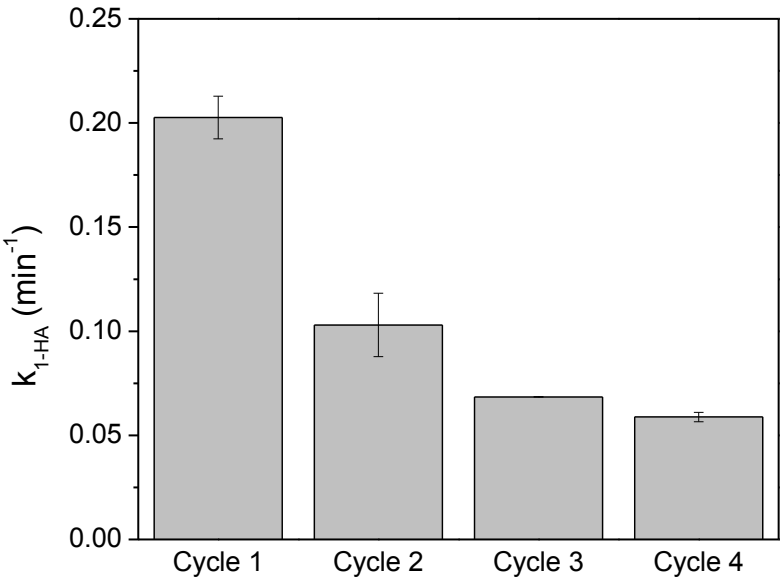

Figure 10 – Pseudo-first-order rate constant for humic acid removal cycling experiments using α-Al_2O_3 (T = 25 ºC; flow rate of ozone = 0.063 m^3 h-1; $[HA]_0$ = 50 mg L^{-1}, $[Al_2O_3]$ = 0.5 g L^{-1}, pH = 5.5).

FTIR analysis of the α-Al_2O_3 catalysts before and after the cyclic tests (Figure 11) was performed to investigate the mechanism of catalyst deactivation. The

absorption band at 500-600 cm^{-1} of α-Al_2O_3 (Figure 11a) is due to Al-O stretching vibration and appears in all samples containing α-Al_2O_3: after HAs adsorption (Figure 11d), after the first cycle (Figure 11b) and after the fourth cycle (Figure 11c). The typical FTIR spectrum of pure HAs (Figure 11, trace e) presents a broad absorption peak at 3500–3400 cm^{-1} attributed to C=C stretching in the aromatic rings and O-H stretching in the alcohols and phenols, and a comparatively sharp absorption peak at 1618 cm^{-1} arising from the skeletal vibration of C=C in the aromatic rings or C=O stretching in quinones. A similar spectrum was obtained after HAs adsorption on the α-Al_2O_3 surface (Figure 11, trace d), although the peaks in the range 600 – 1000 cm^{-1} decreased after consecutive cycles (Figures 11c) with a tendency to match the patterns of the the fresh α-Al_2O_3 sample (Figure 11a). This behavior could be related to the continuous renewal of the catalyst surface due to the reaction catalytic decomposition of ozone on the surface of the catalyst and reaction of ROS with HAs on the solid surface and/or desorption of HAs.

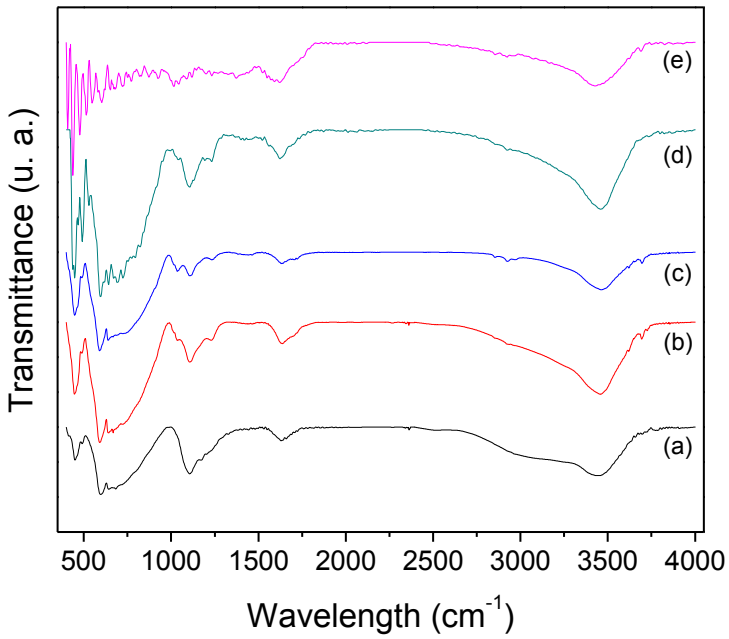

Figure 11 - FTIR vibrational absorption spectra for (a) α-Al_2O_3; (b) and (c) α- Al_2O_3 after 1 and 4 cycles, respectively; (d) α-Al_2O_3 after adsorption of HAs and (e) pure HAs. Adsorption in the presence or absence of ozone conditions: T = 25 ºC; flow rate of ozone = 0.063 $m^3\ h^{-1}$; $[HA]_0$ = 50 mg L^{-1}, $[Al_2O_3]$=0.5 g L^{-1}, pH = 5.5.

4. Conclusions

This study investigated the mechanisms of reaction of ozone with HAs in the presence of α-Al_2O_3 and Mn_2O_3 nanoparticles. The adsorption of HAs, ozone decomposition and the surface reactions are all important factors that control the effective removal of HAs. The results revealed that Mn_2O_3 decomposed ozone more effectively than α-Al_2O_3, but the low surface area and unfavorable adsorption conditions for HAs resulted in slower HAs removal than α-Al_2O_3. pH plays a key role in the catalytic action of both α-Al_2O_3 and Mn_2O_3 nanoparticles. At the natural pH of HAs aqueous solution (pH 5.5) Mn_2O_3 did not exhibited catalytic action during the ozonation of HAs, while a significant catalytic effect was observed with α-Al_2O_3. The mechanism of the HAs removal on α-Al_2O_3 nanoparticles proceeds through adsorption of HAs on the alumina surface, the attack by ozone from either the bulk solution or by the ROS on the catalyst surface and the catalytic decomposition of humic acid on the solid surface. This study, however, showed that the catalytic action of Mn_2O_3 for the removal of NOM by ozonation can be best revealed at pH higher than 5.9, the PZC of Mn_2O_3, and by synthesizing nanoparticles with larger specific surface areas.

Notably, the α-Al_2O_3 dosage (0.1 – 0.5 g L^{-1}) required to remove HAs in the presence of ozone was significantly lower than in other studies, employing granular activated carbon and iron coated zeolite (up to 2 g L^{-1}) or γ-alumina (30 g L^{-1} – 50 g L^{-1}).

The results of this study demonstrated the need of performing in-depth mechanistic studies on the treatment of contaminated water by catalytic ozonation with metal oxides, since NOM is indigenous to most natural water and plays a key role in the removal of other dissolved contaminants of emerging concern.

Acknowledgements

The authors acknowledge CAPES for a scholarship and CNPq for financial support. The authors would like to thank the LCME-UFSC for technical support provided during the electron microscopy work.

References

[1] C. Trellu, Y. Péchaud, N. Oturan, E. Mousset, D. Huguenot, E.D. van Hullebusch, et al., Comparative study on the removal of humic acids from drinking water by anodic oxidation and electro-Fenton processes: Mineralization efficiency and modelling, Appl. Catal. B Environ. 194 (2016) 32–41. doi:10.1016/J.APCATB.2016.04.039.

[2] D. Gümüş, F. Akbal, A comparative study of ozonation, iron coated zeolite catalyzed ozonation and granular activated carbon catalyzed ozonation of humic acid, Chemosphere. 174 (2017) 218–231. doi:10.1016/J.CHEMOSPHERE.2017.01.106.

[3] S.W. Krasner, W.A. Mitch, D.L. McCurry, D. Hanigan, P. Westerhoff, Formation, precursors, control, and occurrence of nitrosamines in drinking water: A review, Water Res. 47 (2013) 4433–4450. doi:10.1016/J.WATRES.2013.04.050.

[4] M.J. McGuire, R.G. Meadow, AWWARF trihalomethane survey., J. / Am. Water

Work. Assoc. 80 (1988) 61–68.

[5] R. Rosal, A. Rodríguez, M. Zerhouni, Enhancement of gas–liquid mass transfer during the unsteady-state catalytic decomposition of ozone in water, Appl. Catal. A Gen. 305 (2006) 169–175. doi:10.1016/J.APCATA.2006.02.059.

[6] B. Seredyńska-Sobecka, M. Tomaszewska, A.W. Morawski, Removal of humic acids by the ozonation–biofiltration process, Desalination. 198 (2006) 265–273. doi:10.1016/J.DESAL.2006.01.027.

[7] T. Ratpukdi, S. Siripattanakul, E. Khan, Mineralization and biodegradability enhancement of natural organic matter by ozone–VUV in comparison with ozone, VUV, ozone–UV, and UV: Effects of pH and ozone dose, Water Res. 44 (2010) 3531–3543. doi:10.1016/J.WATRES.2010.03.034.

[8] M.R. Assalin, N. Dúran, Novas tendências para aplicação de ozônio no tratamento de resíduos : ozonização catalítica, Revista Analytica. 26 (2007) 76–86.

[9] A. Ikhlaq, D.R. Brown, B. Kasprzyk-Hordern, Catalytic ozonation for the removal of organic contaminants in water on alumina, Appl. Catal. B Environ. 165 (2015) 408–418. doi:10.1016/J.APCATB.2014.10.010.

[10] P.C.C. Faria, J.J.M. Órfão, M.F.R. Pereira, Activated carbon catalytic ozonation of oxamic and oxalic acids, Appl. Catal. B Environ. 79 (2008) 237–243. doi:10.1016/J.APCATB.2007.10.021.

[11] B. Kasprzyk-Hordern, U. Raczyk-Stanisławiak, J. Świetlik, J. Nawrocki, Catalytic ozonation of natural organic matter on alumina, Appl. Catal. B Environ.

62 (2006) 345–358. doi:10.1016/J.APCATB.2005.09.002.

[12] A. Ikhlaq, D.R. Brown, B. Kasprzyk-Hordern, Mechanisms of catalytic ozonation: An investigation into superoxide ion radical and hydrogen peroxide formation during catalytic ozonation on alumina and zeolites in water, Appl. Catal. B Environ. 129 (2013) 437–449. doi:10.1016/J.APCATB.2012.09.038.

[13] F. Nawaz, Y. Xie, J. Xiao, H. Cao, Z.A. Ghazi, Z. Guo, et al., The influence of the substituent on the phenol oxidation rate and reactive species in cubic MnO_2 catalytic ozonation, Catal. Sci. Technol. 6 (2016) 7875–7884. doi:10.1039/C6CY01542E.

[14] R.C. Martins, R.M. Quinta-Ferreira, Catalytic ozonation of phenolic acids over a Mn–Ce–O catalyst, Appl. Catal. B Environ. 90 (2009) 268–277. doi:10.1016/J.APCATB.2009.03.023.

[15] R.C. Martins, R.M. Quinta-Ferreira, Phenolic wastewaters depuration and biodegradability enhancement by ozone over active catalysts, Desalination. 270 (2011) 90–97. doi:10.1016/J.DESAL.2010.11.026.

[16] F. Qi, B. Xu, Z. Chen, L. Zhang, P. Zhang, D. Sun, Mechanism investigation of catalyzed ozonation of 2-methylisoborneol in drinking water over aluminum (hydroxyl) oxides: Role of surface hydroxyl group, Chem. Eng. J. 165 (2010) 490–499. doi:10.1016/j.cej.2010.09.047.

[17] J. Nawrocki, Catalytic ozonation in water: Controversies and questions. Discussion paper, Appl. Catal. B Environ. 142–143 (2013) 465–471. doi:10.1016/j.apcatb.2013.05.061.

[18] J. Nawrocki, L. Fijołek, Effect of aluminium oxide contaminants on the process of ozone decomposition in water, Appl. Catal. B Environ. 142–143 (2013) 533–537. doi:10.1016/J.APCATB.2013.05.069.

[19] J. Nawrocki, B. Kasprzyk-Hordern, The efficiency and mechanisms of catalytic ozonation, Appl. Catal. B Environ. 99 (2010) 27–42. doi:10.1016/J.APCATB.2010.06.033.

[20] O. Turkay, H. Inan, A. Dimoglo, Experimental study of humic acid degradation and theoretical modelling of catalytic ozonation, Environ. Sci. Pollut. Res. 22 (2015) 202–210. doi:10.1007/s11356-014-3326-5.

[21] K.C. Chen, Y.H. Wang, The effects of Fe-Mn oxide and TiO_2/α-Al_2O_3 on the formation of disinfection by-products in catalytic ozonation, Chem. Eng. J. 253 (2014) 84–92. doi:10.1016/j.cej.2014.04.111.

[22] Q. Wang, Z. Yang, B. Chai, S. Cheng, X. Lu, X. Bai, Heterogeneous catalytic ozonation of natural organic matter with goethite, cerium oxide and magnesium oxide, RSC Adv. 6 (2016) 14730–14740. doi:10.1039/c5ra21674e.

[23] T. Zhang, J. Lu, J. Ma, Z. Qiang, Comparative study of ozonation and synthetic goethite-catalyzed ozonation of individual NOM fractions isolated and fractionated from a filtered river water, Water Res. 42 (2008) 1563–1570. doi:10.1016/J.WATRES.2007.11.005.

[24] A. Ikhlaq, D.R. Brown, B. Kasprzyk-Hordern, Mechanisms of catalytic ozonation on alumina and zeolites in water: Formation of hydroxyl radicals, Appl. Catal. B Environ. 123–124 (2012) 94–106. doi:10.1016/J.APCATB.2012.04.015.

[25] F. Qi, Z. Chen, B. Xu, J. Shen, J. Ma, C. Joll, et al., Influence of surface texture and acid–base properties on ozone decomposition catalyzed by aluminum (hydroxyl) oxides, Appl. Catal. B Environ. 84 (2008) 684–690. doi:10.1016/J.APCATB.2008.05.027.

[26] F. Qi, B. Xu, Z. Chen, J. Ma, D. Sun, L. Zhang, Influence of aluminum oxides surface properties on catalyzed ozonation of 2,4,6-trichloroanisole, Sep. Purif. Technol. 66 (2009) 405–410. doi:10.1016/J.SEPPUR.2009.01.013.

[27] American Public Health Association, American Water Works Association, Water Environment Federation, Standard methods for the examination of water and wastewater, 19th ed., American Public Health Association, Washington DC, 1995.

[28] D.E. Sullivan, J.A. Roth, Kinetics of ozone self-decomposition in aqueous solution, AIChE Symp. Ser. 76 (1979) 142–149.

[29] F.J. Beltrán, Ozone Reaction Kinetics for Water and Wastewater Systems, CRC Press, 2003. doi:10.1201/9780203509173.

[30] J.L. Sotelo, F.J. Beltran, F.J. Benitez, J. Beltran-heredia, Ozone Decomposition in Water: Kinetic Study, Ind. Eng. Chem. Res. 26 (1987) 39–43. doi:10.1021/ie00061a008.

[31] T. Mizuno, H. Tsuno, H. Yamada, Development of Ozone Self-Decomposition Model for Engineering Design, Ozone Sci. Eng. 29 (2007) 55–63. doi:10.1080/01919510601115849.

[32] J.A. Roth, D.E. Sullivan, Solubility of ozone in water, Ind. Eng. Chem. Fundam.

20 (1981) 137–140. doi:10.1021/i100002a004.

[33] P.-C. Li, C.-C. Hu, H. Noda, H. Habazaki, Synthesis and characterization of carbon black/manganese oxide air cathodes for zinc–air batteries: Effects of the crystalline structure of manganese oxides, J. Power Sources. 298 (2015) 102–113. doi:10.1016/J.JPOWSOUR.2015.08.051.

[34] E.P. Barrett, L.G. Joyner, P.P. Halenda, The Determination of Pore Volume and Area Distributions in Porous Substances. I. Computations from Nitrogen Isotherms, J. Am. Chem. Soc. 73 (1951) 373–380. doi:10.1021/ja01145a126.

[35] J. Haber, Manual on catalyst characterization (Recommendations 1991), Pure Appl. Chem. 63 (1991) 1227–1246. doi:10.1351/pac199163091227.

[36] K.S.W. Sing, Reporting physisorption data for gas/solid systems with special reference to the determination of surface area and porosity (Provisional), Pure Appl. Chem. 54 (1982) 2201–2218. doi:10.1351/pac198254112201.

[37] A.W. Burton, K. Ong, T. Rea, I.Y. Chan, On the estimation of average crystallite size of zeolites from the Scherrer equation: A critical evaluation of its application to zeolites with one-dimensional pore systems, Microporous Mesoporous Mater. 117 (2009) 75–90. doi:10.1016/J.MICROMESO.2008.06.010.

[38] N. Salahudeen, A.S. Ahmed, A.H. Al-Muhtaseb, M. Dauda, S.M. Waziri, B.Y. Jibril, et al., Synthesis, characterization and adsorption study of nano-sized activated alumina synthesized from kaolin using novel method, Powder Technol. 280 (2015) 266–272. doi:10.1016/J.POWTEC.2015.04.024.

[39] B.C. Sekhar, N. Kalaiselvi, Pristine hollow microspheres of Mn_2O_3 as a potential

anode for lithium-ion batteries, CrystEngComm. 17 (2015) 5038–5045. doi:10.1039/C5CE00465A.

[40] M.K. Trivedi, G. Nayak, S. Patil, R.M. Tallapragada, O. Latiyal, Evaluation of Biofield Treatment on Physical, Atomic and Structural Characteristics of Manganese (II, III) Oxide, J. Mater. Sci. Eng. 04 (2015) 1–6. doi:10.4172/2169-0022.1000177.

[41] P.K. Kiyohara, H.S. Santos, A.C.V. Coelho, P. de S. Santos, Structure, surface area and morphology of aluminas from thermal decomposition of $Al(OH)(CH_3COO)_2$ crystals, An. Acad. Bras. Cienc. 72 (2000) 471–495. doi:10.1590/S0001-37652000000400003.

[42] H.S. Kim, N.-K. Park, T.J. Lee, M.-H. Um, M. Kang, Preparation of Nanosized alfa-Al_2O_3 Particles Using a Microwave Pretreatment at Mild Temperature, Adv. Mater. Sci. Eng. 2012 (2012) 1–6. doi:10.1155/2012/920105.

[43] Y. Hu, H. Qian, C. Guo, T. Mei, Decoration of ZnO nanocrystals on the surface of shuttle-shaped Mn_2O_3 and its magnetic-optical properties, CrystEngComm. 12 (2010) 2687. doi:10.1039/b924820j.

[44] S. Zhan, D. Zhu, M. Qiu, H. Yu, Y. Li, Highly efficient removal of NO with ordered mesoporous manganese oxide at low temperature, RSC Adv. 5 (2015) 29353–29361. doi:10.1039/C4RA17300G.

[45] S.C. Reiff, J.A. LaVerne, Radiolysis of water with aluminum oxide surfaces, Radiat. Phys. Chem. 131 (2017) 46–50. doi:10.1016/J.RADPHYSCHEM.2016.10.022.

[46] J. Oh, S. Shin, J. Park, G. Ham, H. Jeon, Characteristics of Al_2O_3/ZrO_2 laminated films deposited by ozone-based atomic layer deposition for organic device encapsulation, Thin Solid Films. 599 (2016) 119–124. doi:10.1016/J.TSF.2015.12.044.

[47] A.P.S.L. Centurião, V.Z. Baldissarelli, G. Scaratti, S.M. de Amorim, R.F.P.M. Moreira, Enhanced ozonation degradation of petroleum refinery wastewater in the presence of oxide nanocatalysts, Environ. Technol. (2018) 1–11. doi:10.1080/09593330.2017.1420103.

[48] M.C. Biesinger, B.P. Payne, A.P. Grosvenor, L.W.M. Lau, A.R. Gerson, R.S.C. Smart, Resolving surface chemical states in XPS analysis of first row transition metals, oxides and hydroxides: Cr, Mn, Fe, Co and Ni, Appl. Surf. Sci. 257 (2011) 2717–2730. doi:10.1016/J.APSUSC.2010.10.051.

[49] H. Zhu, Z. Shen, Q. Tang, W. Ji, L. Jia, Degradation mechanism study of organic pollutants in ozonation process by QSAR analysis, Chem. Eng. J. 255 (2014) 431–436. doi:10.1016/J.CEJ.2014.05.073.

[50] M. Ernst, F. Lurot, J.-C. Schrotter, Catalytic ozonation of refractory organic model compounds in aqueous solution by aluminum oxide, Appl. Catal. B Environ. 47 (2004) 15–25. doi:10.1016/S0926-3373(03)00290-X.

[51] W. Li, G. V. Gibbs, S.T. Oyama, Mechanism of ozone decomposition on a manganese oxide catalyst. 1. In situ Raman spectroscopy and Ab initio molecular orbital calculations, J. Am. Chem. Soc. 120 (1998) 9041–9046. doi:10.1021/ja981441+.

[52] M.E. Lovato, C.A. Martín, A.E. Cassano, A reaction kinetic model for ozone

decomposition in aqueous media valid for neutral and acidic pH, Chem. Eng. J. 146 (2009) 486–497. doi:10.1016/J.CEJ.2008.11.001.

[53] Am Water Works Res F, Ozone in Water Treatment: Application and Engineering, 1 st, CRC Press, 1991.

[54] W. Li, S.T. Oyama, Mechanism of ozone decomposition on a manganese oxide catalyst 2. Steady-state and transient kinetic studies, J. Am. Chem. Soc. 120 (1998) 9047–9052. doi:10.1021/ja9814422.

[55] H. Miao, W. Tao, Ozonation of humic acid in water, J. Chem. Technol. Biotechnol. 83 (2008) 336–344. doi:10.1002/jctb.1816.

[56] N. Janot, P.E. Reiller, X. Zheng, J.P. Croué, M.F. Benedetti, Characterization of humic acid reactivity modifications due to adsorption onto α-Al_2O_3, Water Res. 46 (2012) 731–740. doi:10.1016/j.watres.2011.11.042.

[57] T. Tanaka, Functional groups and reactivity of size-fractionated Aldrich humic acid, Thermochim. Acta. 532 (2012) 60–64. doi:10.1016/J.TCA.2011.12.004.

Supplementary Material_revised

Click here to download Supplementary Material: Sup Material_Rev.docx